Proceedings of the Project Review, Geo-Mathematical Imaging Group (Purdue University, West Lafayette IN), Vol. 1 (2011) pp. 243-252.

MODELING OF SEISMIC WAVE SCATTERING FROM ROUGH FRACTURE SURFACES

CHRISTOPHER L. PETROVITCH*, LAURA J. PYRAK-NOLTE†, AND MAARTEN V. DE HOOP‡

Abstract. The Runge-Kutta Discontinuous Galerkin method (RKDG) is presented for the isotropic elastic wave equation and shown to have higher than second-order convergence. The method was then used to predict seismic scattering fields caused by different two dimensional rock fractures. In this study, shear-waves were numerically propagated parallel to a fractured sample of Austin Chalk in order to show the methods ability to generate fracture interface waves.

1 Introduction A fundamental understanding of the earth's subsurface is of upmost concern to todays' society such as, extraction of drinkable water, the production of oil & gas, construction of subsurface structures (tunnels and foundations of dams and bridges) and carbon sequestration in subsurfaces reservoirs. The success of these projects relies strongly on a firm understanding of the existing geological structure. Reliable risk assessment must also account for the long term effects of geological processes that occur in the subsurface. A difficulty in characterizing the subsurface arises it is composed of a hierarchy of structures and processes that span a wide range length and time scales.

Fractures are mechanical discontinuities that are present at all length scales. Mechanical discontinuities range in size from lattice dislocations (10^{-9} m) to micro-cracks (10^{-6} m) to fractures (1 m) to the scale of plate boundaries (10^4 m). Any single site will encompass mechanical discontinuities over several orders of magnitude. They dominate the flow of fluids and the mechanical behavior of all subsurface structures and processes. Therefore, it is imperative to be able to characterize them at all scales, and to understand the coupling of the mechanical properties to the fluid flow properties. One of the most prominently used methods to characterize fractures remotely is analyzing the transmission across and reflection off of fractures i.e. the scattered wave field. The dynamic stiffness of a fracture can be estimated by using the Displacement-Discontinuity (DD) theory, Pyrak-Nolte et. al. [13]. In this study, the authors intend to display a powerful computational model to aid in the understanding of the scattered wave fields associated with rock fractures.

There are several computational methods used to calculate the scattering field of a rock fracture. To the author's knowledge, single fractures are normally modeled as planes with a constant stiffness. When viewing a fracture in this way, one can apply the DD theory to calculate a boundary condition at the fracture plane. However the constant stiffness requirement was overcome by Nakagawa et al. [11] and Nihei et al. [12]. These boundary condition has been used in Finite Difference and Finite Element methods to a great extent, however the requirements are very demanding. The stiffness variation across the fracture plane must be low and the fracture must be planar. In nature, there are many occurrences where these requirements cannot be met.

The Discontinuous Galerkin (DG) approximation was selected to model the problem because it combinds the meshing flexibility of classical FE methods with the ability to easily calculate high-order solutions.

*Department of Physics, Purdue University, West Lafayette, Indiana, USA
†Department of Physics, Purdue University, West Lafayette, Indiana, USA, and Department of Earth and Atmospheric Physics, Purdue University, West Lafayette, Indiana, USA
‡ Center for Computational and Applied Mathematics, and Geo-Mathematical Imaging Group, Purdue University, West Lafayette, IN 47907, USA.

2 Computational Model To simulate seismic wave scattering, we begin with the two dimensional elastic wave equation,

$$\begin{aligned}
\frac{\partial}{\partial t}\sigma_{xx} - (\lambda+2\mu)\frac{\partial}{\partial x}v_x - \lambda\frac{\partial}{\partial y}v_y &= 0 \\
\frac{\partial}{\partial t}\sigma_{yy} - \lambda\frac{\partial}{\partial x}v_x - (\lambda+2\mu)\frac{\partial}{\partial y}v_y &= 0 \\
\frac{\partial}{\partial t}\sigma_{xy} - \mu\left(\frac{\partial}{\partial x}v_y - \frac{\partial}{\partial y}v_x\right) &= 0 \\
\rho\frac{\partial}{\partial t}v_x - \frac{\partial}{\partial x}\sigma_{xx} - \frac{\partial}{\partial y}\sigma_{xy} &= 0 \\
\rho\frac{\partial}{\partial t}v_y - \frac{\partial}{\partial x}\sigma_{xy} - \frac{\partial}{\partial y}\sigma_{yy} &= 0,
\end{aligned} \tag{2.1}$$

where σ_{ij} are the stress tensor components, v_i are the velocity components and (λ, μ, ρ) are the Lamé parameters and density that define the material properties of the domain. Equation 2.1 is an example of a linear hyperbolic equation and can be rewritten into a more compact form,

$$\frac{\partial Q_p}{\partial t} + A_{pq}\frac{\partial Q_q}{\partial x} + B_{pq}\frac{\partial Q_q}{\partial y} = 0 \tag{2.2}$$

with $Q_p = [\sigma_{xx}, \sigma_{yy}, \sigma_{xy}, v_x, v_y]^T$ and (A_{pq}, B_{pq}) are the constant coefficient matrices which create Equation 2.1. To numerically compute solutions this system of equations, the Discontinuous Galerkin method (DG) was used to discretize the spatial derivatives and the Total Variation Diminishing Runge-Kutta method (TVD-RK) [16] was used to step the solution in time.

2.1 Spatial discretization via the DG Method To derive the semi-discrete discontinuous galerkin (DG) formulation, we assume that the domain is defined by a finite number of smaller elements either by hand or meshing software such as *Triangle* [15]. In this study, only conforming meshes of straight sided triangles were used because geometries considered in this paper do not require curved boundaries.

The solution over any given triangle, $\mathcal{T}^{(m)}$, is represented by a linear combination of modal basis functions that are solely space-dependent. Following the spirit of Dumbser & Käser [6], the derivation of the semi-discrete form begins like all finite element methods, by expanding the solution into an appropriate basis,

$$\left[Q_h^{(m)}\right]_p(\xi,\eta) = \hat{Q}_{pl}^{(m)}(t)\Phi_l(\xi,\eta), \tag{2.3}$$

where the basis functions, $\Phi_l(\xi,\eta)$, are the Jacobi polynomials, found in Cockburn *et al.* [4]. Also, the subscripts h, p, and l indicate the numerical solution, the element in the unknown state vector, and the l^{th} basis function, respectively. Then Equation 2.2 is multiplied by a test function, Φ_k, and integrated over the elements volume.

$$\int_{\mathcal{T}^{(m)}} \Phi_k \frac{\partial Q_p}{\partial t} dV + \int_{\mathcal{T}^{(m)}} \Phi_k \left(A_{pq}\frac{\partial Q_q}{\partial x} + B_{pq}\frac{\partial Q_q}{\partial y}\right) dV = 0$$

Integrating by parts reveals the weak form of the seismic wave equation,

$$\int_{\mathcal{T}^{(m)}} \Phi_k \frac{\partial Q_p}{\partial t} dV - \int_{\mathcal{T}^{(m)}} \left(\frac{\partial \Phi_k}{\partial x}A_{pq}Q_q + \frac{\partial \Phi_k}{\partial y}B_{pq}Q_q\right) dV + \int_{\partial\mathcal{T}^{(m)}} \Phi_k F_p^h dS = 0. \tag{2.4}$$

Note that the boundary term (last term) is non-zero as oppose to classical FEM and the numerical flux is introduced, F_p^h. The flux term defines how information travels from element to element and

plays a critical role in the stability of the method. As shown in Dumbser & Käser [6], an upwinding Godunov flux provides acceptable convergence and stability. It is derived in Leveque's textbook on Finite Volume methods [8]. The flux is written as follows,

$$\begin{aligned} F_p^h = &\frac{1}{2}T_{pq}\left(A_{qr}^{(m)} + \left|A_{qr}^{(m)}\right|\right)T_{rs}^{-1}\hat{Q}_{sl}^{(m)}\Phi_l^{(m)} + \\ &\frac{1}{2}T_{pq}\left(A_{qr}^{(m)} - \left|A_{qr}^{(m)}\right|\right)T_{rs}^{-1}\hat{Q}_{sl}^{(m_j)}\Phi_l^{(m_j)}, \end{aligned} \tag{2.5}$$

where the superscript (m_j) refers to the j^{th} neighbor of m, T_{ij} is a rotation matrix such that the boundary in question is rotated into an *edge-aligned* coordinate system (Equation 2.6), and the notation of $|A_{ij}^{(m)}|$ refers to applying the absolute value to the eigenvalues of A_{ij}, with material properties associated with $\mathcal{T}^{(m)}$,

$$|A_{pq}| = R_{pr}^A\,|\Lambda_{rs}|\,(R_{sq})^{-1}, \qquad \text{with} \quad |\Lambda_{rs}| = \mathrm{diag}(|\alpha_1|, |\alpha_2|, \ldots),$$

where α_i are the eigenvalues of A_{ij} and R_{ij}^A is a matrix with eigenvectors as columns. Also, the transformation matrix can be written as follows,

$$T_{ij} = \begin{bmatrix} n_x^2 & n_y^2 & -2n_xn_y & 0 & 0 \\ n_y^2 & n_x^2 & 2n_xn_y & 0 & 0 \\ n_xn_y & -n_xn_y & n_x^2 - n_y^2 & 0 & 0 \\ 0 & 0 & 0 & n_x & -n_y \\ 0 & 0 & 0 & n_y & n_x \end{bmatrix}, \tag{2.6}$$

where $\vec{n} = (n_x, n_y)$ is the outward pointing normal vector of the edge in question.

Now, by transforming the integrals to a reference triangle, $\mathcal{T}_E$, and expanding the solution, Q_p into the basis defined above, we obtain the DG semi-discrete form of the elastic wave equation,

$$\begin{aligned} &\frac{\partial}{\partial t}\hat{Q}_{pl}^{(m)}|J|M_{lk} + \sum_{j=1}^{3}\frac{1}{2}T_{pq}\left(A_{qr}^{(m)} + \left|A_{qr}^{(m)}\right|\right)T_{rs}^{-1}\hat{Q}_{sl}^{(m)}|S_j|F_{lk}^{j,0} \\ &+ \sum_{j=1}^{3}\frac{1}{2}T_{pq}\left(A_{qr}^{(m)} - \left|A_{qr}^{(m)}\right|\right)T_{rs}^{-1}\hat{Q}_{sl}^{(m_j)}|S_j|F_{lk}^{j,i} \\ &- A_{pq}^*\hat{Q}_{ql}^{(m)}|J|K_{lk}^{\xi} - B_{pq}^*\hat{Q}_{ql}^{(m)}|J|K_{lk}^{\eta} = 0, \end{aligned} \tag{2.7}$$

where $|S_j|$ is the length of edge j, $|J|$ is the area of element m, and the matrices M_{lk}, K_{lk}^{ξ}, K_{lk}^{η}, $F_{lk}^{j,0}$, $F_{lk}^{j,i}$, A_{pq}^*, and B_{pq}^* are defined as follows:

$$M_{lk} = \int_{\mathcal{T}_E}\Phi_l\Phi_k d\xi d\eta \tag{2.8}$$

$$K_{lk}^{\xi} = \int_{\mathcal{T}_E}\frac{\partial\Phi_l}{\partial\xi}\Phi_k d\xi d\eta \tag{2.9}$$

$$K_{lk}^{\eta} = \int_{\mathcal{T}_E}\frac{\partial\Phi_l}{\partial\eta}\Phi_k d\xi d\eta \tag{2.10}$$

$$F_{lk}^{j,0} = \int_0^1\Phi_l^{(m)}(\chi_j)\Phi_k^{(m)}(\chi_j)d\chi_j \tag{2.11}$$

$$F_{lk}^{j,i} = \int_0^1\Phi_l^{(m)}(\chi_j)\Phi_k^{(m_j)}(\hat{\chi}_i)d\chi_j \tag{2.12}$$

$$A_{pq}^* = A_{pq}\frac{\partial\xi}{\partial x} + B_{pq}\frac{\partial\xi}{\partial y} \tag{2.13}$$

$$B_{pq}^* = A_{pq}\frac{\partial\eta}{\partial x} + B_{pq}\frac{\partial\eta}{\partial y} \tag{2.14}$$

where χ_j is a parameterization of face j of the current element, $\mathcal{T}^{(m)}$. Also noting that when integrating over the surface in $F_{lk}^{j,i}$, two parameterizations must be used with the relation $\hat{\chi}_i = 1-\chi_i$. Therefore, the 15 matrices (Equations 2.8-2.12) can be tabulated beforehand on a algebraic software package. This leads to a completely quadrature free implementation of the seismic wave equation.

It is important to note that the semi-discrete form (Equation 2.7) is completely localized, i.e. each element m is calculated solely by its current solution of itself and its three neighbors. This is only possible because the elements are no longer required to be continuous. Localization has many benefits such as: (1) there is no need to construct a global matrix, as in FEM, (2) it allows for simple parallelization , and (3) p-Adaptivity is easily obtained. Because there are no global matrices, the DG method can obtain very high order solutions without the worry of causing the condition number of the mass matrix (which must be inverted) to grow uncontrollably. It also allows the implementation (in the source code) to be written with the simplicity of a FD code, updating each element one at a time. Lastly, the semi-discrete form above is already p-Adaptive, meaning each element can have its own approximation order. The difference is simple in that the matrices (Equations 2.11 & 2.12) will become non-square in the event of a neighboring element having a different order rather than $N_p \times N_p$, where $N_p = (N+1)(N+2)/2$ and N is the order of approximation. For these reasons, the DG method is a very powerful computational tool for simulating the seismic wave equation.

2.2 TVD Runge-Kutta Time-stepping The solution vector in the semi-discrete form (Equation 2.7) is propagated forward in time by a three stage TVD-RK method [16]. This method was chosen because it reduces artificial oscillatory motion of linear hyperbolic equations and reduces errors caused near discontinuities in a solution. The TVD-RK method sets out to discretize the ODE,

$$u_t = \mathcal{L}(u)$$

where in the case of this paper, $\mathcal{L}(u)$ can be found by solving for the time derivative on $\hat{Q}_{pl}$ in Equation 2.7. To integrate from u^n to u^{n+1}, where the superscript represents the time step, the TVD-RK method is as follows,

$$\begin{aligned} k^{(0)} &= u^n \\ k^{(1)} &= k^{(0)} + \Delta t \mathcal{L}(k^{(0)}) \\ k^{(2)} &= \frac{3}{4}k^{(0)} + \frac{1}{4}k^{(1)} + \frac{1}{4}\Delta t \mathcal{L}(k^{(1)}) \\ u^{n+1} &= \frac{1}{3}k^{(0)} + \frac{2}{3}k^{(2)} + \frac{2}{3}\Delta t \mathcal{L}(k^{(2)}). \end{aligned} \tag{2.15}$$

In examples [6, 1] the authors found the CFL condition to be similar to other DG-RK implementations. The choice of time step, Δt, must hold to the condition,

$$c\frac{\Delta t}{\Delta x} \leq \frac{1}{2N+1}$$

where c is the fastest wave speed in the domain, Δx is the diameter of the circumscribed circle on the smallest element in the mesh, and N is the order of the spatial approximation, $N = p+1$.

Combining the spatial and temporal discretization (Equations 2.7 & 2.15), we have a complete numerical platform to compute scattering fields of elastic waves in complex mediums.

3 Convergence Study: Free Surface The accuracy and stability of method were tested along with the free-surface boundary condition. In this example, an eigenmode of the system was propagated in a homogeneous medium. The computational domain Ω is a unit square ($[0,1] \times [0,1]$) with free surface boundary conditions on all four sides. The medium properties were set such that the compressional and shear wave speeds were $v_p = 1\ m/s$ and $v_s = 0.5\ m/s$, respectively. This

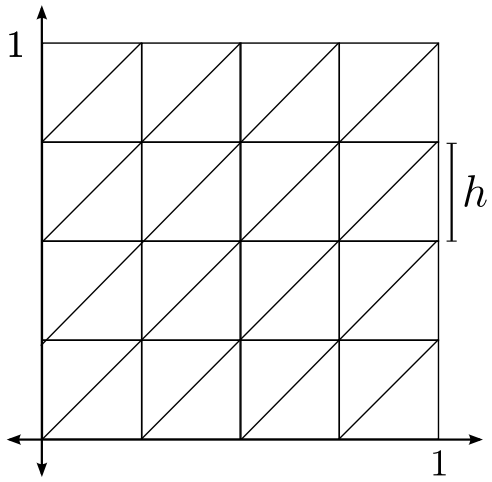

FIG. 1. *Example mesh showing the refinement parameter,* $h = \frac{1}{4}$.

means that the material properties in each element was set to $(\rho, \lambda, \mu) = \left(1 \text{ kg/m}^3, 0.5 \text{ Pa}, 0.25 \text{ Pa}\right)$. The exact analytic solution is,

$$
\begin{aligned}
v_x &= \quad \sqrt{2}\pi v_s \cos(\pi x)\sin(\pi y)\cos(\sqrt{2}\pi v_s t) \\
v_y &= -\sqrt{2}\pi v_s \sin(\pi x)\cos(\pi y)\cos(\sqrt{2}\pi v_s t) \\
\sigma_{xx} &= -2\pi\mu \sin(\pi x)\sin(\pi y)\sin(\sqrt{2}\pi v_s t) \\
\sigma_{yy} &= \quad 2\pi\mu \sin(\pi x)\sin(\pi y)\sin(\sqrt{2}\pi v_s t) \\
\sigma_{xy} &= 0.
\end{aligned} \tag{3.1}
$$

The domain was meshed with a regular triangular mesh by breaking the unit square into a $N \times N$ grid, where each grid cell was divided into triangles (Figure 1). Two refinements were done to observe the convergence rate, h-refinement and p-refinement. h-Refinement is when smaller and smaller mesh elements are used to cover the domain, i.e. the $N \times N$ grid was refined for N = 5, 9, 12, 15, 18 so that the edge length of each element was $h = 1/N$. p-Refinement is when, for a given mesh with fixed N, the polynomial order, p, of the approximation over each element is allowed to grow. For this study, the approximation order ranged from p = 1 to 4.

The results of the convergence analysis are shown in Figure 2. The error was estimated via the L_2 norm defined as follows,

$$
||u_h - u||_2 = \left(\int_\Omega (u_h - u)^2 dV \right)^{1/2}, \tag{3.2}
$$

where u is the analytic solution (Equation 3.1) and u_h is the calculated solution via the DG method. Gaussian quadrature was used to preform the integration over each element of the mesh such that the error would be much less than the simulation. The v_y component of the solution was chosen arbitrarily to calculate the error. The solid dashed line on the left hand side of Figure 2 illustrates second order convergence. It is easily observed that each polynomial approximation achieved second order convergence under mesh refinement. However, it can also be seen that the convergence rate begins to plateau once the polynomial order exceeds three. This is depicted in the right hand side of Figure 2. This graph shows the L_2 error as a function of polynomial order while fixing the mesh refinement. Once the polynomial order reaches three, the error in the TVD-RK time integration grows beyond the DG framework.

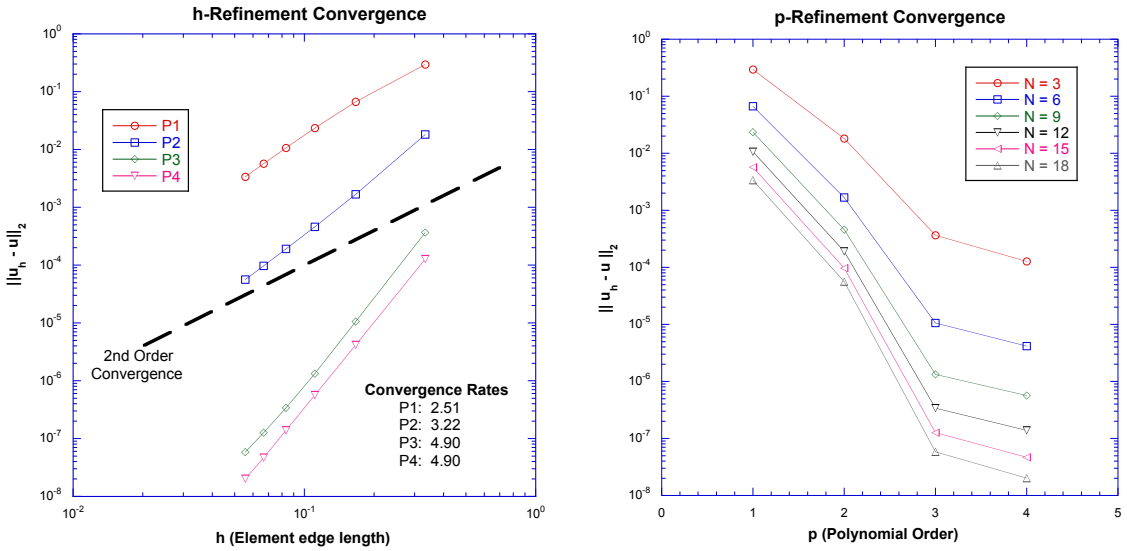

FIG. 2. *(Left) L_2 error as a function of h-refinement. (Right) L_2 error as a function of p-refinement.*

4 Rock Fractures In this section, our DG implementation was used to generate fracture interface waves [10, 14, 7, 2, 3]. Interface waves can be viewed physically as a more general form of a Rayleigh wave. In the case of a pure Rayleigh wave, when a wave propagates along the surface of a medium, it generates a second wave with a velocity $0.92v_s$ and contains both longitudinal and transverse particle motion. This wave is called the Rayleigh wave. However, if two rough surfaces are placed in contact, they create mechanical discontinuities in the form of welded areas and void spaces. This is our basic model of a fracture. Now, when the same wave that generated the Rayleigh wave propagates along this interface, Rayleigh waves will be generated at the void spaces while coupling to the opposite side's waves at the welded areas. The arriving interface wave has a velocity that ranges between the classic Rayleigh wave velocity (all void spaces) and the bulk shear wave velocity (all welded area). So, since the void and welded spaces across the fracture plane are controlled by the mechanical properties of the bulk rock and the geometry of void spaces, the interface wave is also defined by by these properties. In other words, interface waves can be thought of as a probe to the mechanical properties of rock fractures. Namely, by observing the velocities of the incoming interface waves, we can deduce the fracture specific stiffness. Fracture interface waves have been theoretically explained via displacement-discontinuity theory by Pyrak-Nolte & Cook [10] and observed experimentally along both natural and synthetic fractures at the laboratory scale [14].

To define the domain in which this interface of welded and void spaces exist, an aperture map of a fracture must be created. In the laboratory, an intact sample of Austin Chalk was fractured and a acrylic cast was made of each side. Then surface roughness measurements were performed and analyzed for each cast to create a map of the void spaces and contact areas created by the two surfaces. Once the aperture map was obtained, a two dimensional slice was taken from the data set and meshed. The wave velocities of the acrylic casts were measured in the lab and found to a have P-wave velocity of $v_p = 2730$ m/s and a S-wave velocity $v_s = 1430$ m/s. The density of the acrylic was $\rho = 1185$ kg/m^3. With these values, the material properties of the mesh, (λ, μ, ρ), were calculated.

From the displacement-discontinuity approach to interface waves [10], the velocity-stiffness relation can be computed. The relation is shown in Figure 3. It is observed that below approximately 10^9 Pa/m, the interface wave will in effect be a Rayleigh wave (all void spaces) and above 10^{14} the interface wave will merge with the initial wavefront (all welded). However, between these limits we observe two interface wave speeds, simply called the fast and slow interface wave. The fast wave

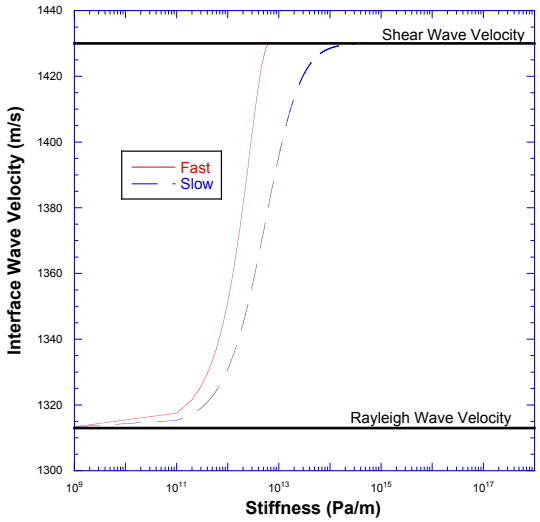

FIG. 3. *Theoretical prediction of stiffnesses from the interface wave velocities. Computed with the material properties of Lucite:* $v_p = 2730$ *m/s,* $v_c = 1430$ *m/s,* $\rho = 1185$ *kg/m*^{3} *and a central frequency 1 MHz.*

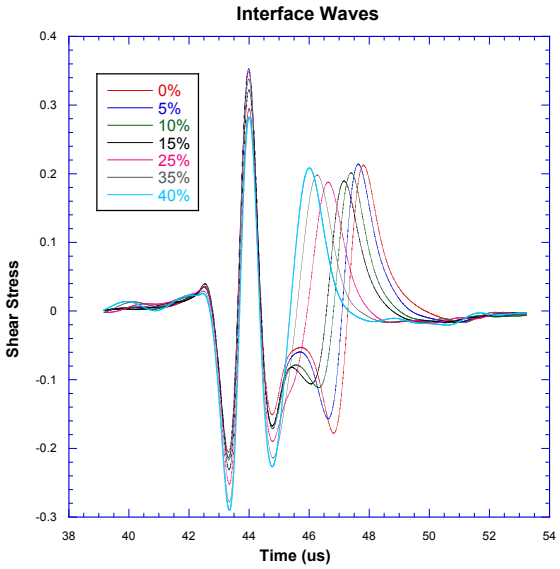

FIG. 4. *Average signal across the fracture plane for differing contact area percentages.*

depends on the normal stiffness while the slow depends on the shear stiffness. While analytically there exists two distinct interface waves, in this study the difference in wave speeds was to small to resolve.

To see the shift in the interface velocity, the fracture was loaded. Numerically, this was done by simply adjusting the percentage of contact area during the meshing phase. While this is not technically a correct loading method, it will illuminate the essential wave physics in the problem. In the future, loading the fracture under a normal load via Hopkins' method [5, 9] is planned. The contact area percentages chosen were: 0%, 5%, 10%, 15%, 25%, 35%, and 40%.

Signals were averaged over 1cm to simulate the data a laboratory transducer would receive. The

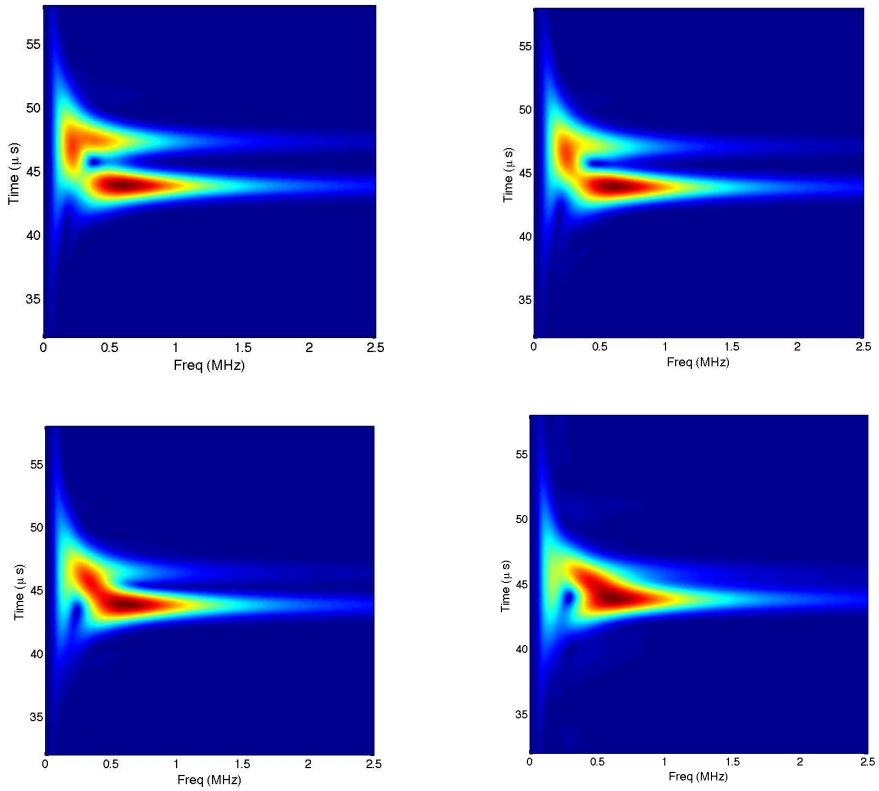

FIG. 5. *Wavelet decompositions of the 0% (top left), 10% (top right), 25% (bottom left), and 40% (bottom right).*

% Contact Area	$v_{interface}$ (m/s)	Stiffness (Pa/m)
0%	1311.7	n/a
5%	1314.9	6.68×10^{9}
10%	1318.2	1.00×10^{11}
15%	1324.8	2.51×10^{11}
25%	1338.2	6.31×10^{11}
35%	1348.4	7.94×10^{11}
40%	1357.6	1.06×10^{12}

TABLE 4.1
Calculated Stiffnesses via the slow interface wave velocities, $v_{interface}$, and displacement-discontinuity theory.

wavefronts are shown in Figure 4. We note that the bulk shear wave arrivals only differ in amplitude while the trailing wave systematically decreases in arrival time when the contact area increases. To calculate the interface wave velocity, arrival times were picked after decomposing the signals into a wavelet basis, Figure 5. From the wavelets, the interface wave can be seen clearly. However, as the contact area increases, the two waves begin to interfere. Therefore using the central frequency of the interface wave becomes rather difficult. The arrival times were picked by taking the 1 MHz slice of each wavelet, where there are still two distinct waves. Table 4.1 lists the interface wave velocities along with their calculated specific stiffnesses.

5 Discussion & Conclusions All in all, a Discontinuous Galerkin formulation has been presented to solve the isotropic elastic wave equation. We demonstrated that the use of the DG

formulation has high convergence rates, exceeding second order convergence. The method is a very flexible and powerful tool because it allows the computational domain to be partitioned over a unstructured mesh where the user may modify element sizes to fit the domain more accurately. p-Adaptivity is also included in the formulation, allowing users to mesh with triangles over a wide range of sizes while keeping the error constant and reducing the computational time. In the future, the authors intend to extend this formulation to three dimensions, allow for local time-stepping of each individual element, and derive a fluid solid boundary condition to allow the study of fluid filled fractures.

REFERENCES

[1] HL Atkins and CW Shu. Quadrature-free implementation of discontinuous Galerkin method for hyperbolic equations. *AIAA JOURNAL*, 36(5):775–782, MAY 1998. AIAA/CEAS 2nd Joint Aeroacoustics Conference, STATE COLL, PENNSYLVANIA, MAY 06-08, 1996.

[2] Gu BL. *Interface Waves on a Fracture in Rock*. PhD thesis, University of California, 1994.

[3] Gu BL, Nihei KT, Myer LR, and Pyrak-Nolte LJ. Fracture interface waves. *Journal of Geophysical Research-Solid Earth*, 1996.

[4] B. Cockburn, G. E. Karniadakis, and C. W. Shu. The development of discontinuous galerkin methods. *Discontinuous Galerkin Methods*, 11:3–50 470, 2000.

[5] Hopkins D.L. *The Effect of Surface Roughness on Joint Stiffness, Aperture, and Acustic Wave Propagation*. PhD thesis, University of California at Berkeley, 1990.

[6] M. Dumbser and M. Kaser. An arbitrary high-order discontinuous galerkin method for elastic waves on unstructured meshes - ii. the three-dimensional isotropic case. *Geophysical Journal International*, 167(1):319–336, 2006.

[7] Murty GS and Kumar V. Elastic wave prpagation with kinematic discontinuity along anon-ideal interface between two isotropic elastic half-spaces. *Journal of Nondestructive Evaluation*, 1991.

[8] R.J. Leveque. *Finite Volume Methods for Hyperbolic Problems*. Cambridge University Press, Cambridge, United Kingdom, 2002.

[9] Pyrak-Nolte LJ and Morris JP. Single fractures under normal stress: The relation between fracture stiffness and fluid flow. *International Journal of Rock Mechanics and Mining Sciences*, 37:245–262, 2000.

[10] Pyrak-Nolte LJ and Cook NGW. Elastic interface waves along a fracture. *Geophysical Research Letters*, 14(11):1107–1110, 1987.

[11] S Nakagawa, KT Nihei, and LR Myer. Plane wave solution for elastic wave scattering by a heterogeneous fracture. *JOURNAL OF THE ACOUSTICAL SOCIETY OF AMERICA*, 115(6):2761–2772, JUN 2004.

[12] KT Nihei. Modeling elastic waves in factured rock with the kirchhoff method. Technical report, Lawrence Berkeley Lab, 1989.

[13] L. J. Pyrak-Nolte, N.G.W. Cook, and L.R. Myer. Transmission of seismic waves across single natural fractures. *Journal of Geophysical Research*, 95:11,345–11,358, 1990.

[14] LJ PYRAKNOLTE, JP XU, and GM HALEY. ELASTIC INTERFACE WAVES PROPAGATING IN A FRACTURE. *PHYSICAL REVIEW LETTERS*, 68(24):3650–3653, JUN 15 1992.

[15] Jonathan Richard Shewchuk. Triangle: Engineering a 2D Quality Mesh Generator and Delaunay Triangulator. In Ming C. Lin and Dinesh Manocha, editors, *Applied Computational Geometry: Towards Geometric Engineering*, volume 1148 of *Lecture Notes in Computer Science*, pages 203–222. Springer-Verlag, May 1996. From the First ACM Workshop on Applied Computational Geometry.

[16] CW SHU and S OSHER. EFFICIENT IMPLEMENTATION OF ESSENTIALLY NON-OSCILLATORY SHOCK-CAPTURING SCHEMES. *JOURNAL OF COMPUTATIONAL PHYSICS*, 77(2):439–471, AUG 1988.